ACS OMEGA

Open Access

http://pubs.acs.org/journal/acsodf

Article

Tailoring Hematite Photoanodes for Improved PEC Performance: The Role of Alcohol Species Revealed by SHAP Analysis

Takumi Idei, Yuya Nagai, Zhenhua Pan, and Kenji Katayama*

Cite This: *ACS Omega* 2024, 9, 44837−44845

Read Online

ACCESS | Metrics & More | Article Recommendations | Supporting Information

ABSTRACT: We explore the synergistic effects of TiO_2 underlayers and varied alcohol species in the precursor solutions on the photoelectrochemical (PEC) performance of hematite photoanodes. Utilizing a robust machine learning (ML) framework combined with comprehensive analytical data sets, we systematically investigate how these modifications influence key physical and chemical properties, directly impacting the efficiency of water splitting processes. Our approach employs an ML model that integrates SHapley Additive exPlanations (SHAP) to quantitatively assess the impact of each dominant descriptor selected in the analytical data on the PEC performance, and they were combined with the SHAP values' dependence on the experimental operations. Specifically, we focus on the type of alcohol (methanol, ethanol, butanol, and 2-ethyl-1-butanol) used in the precursor solutions as the experimental operation, examining their effects on the dominant descriptors selected in the analytical data. The results from the SHAP analysis reveal that different alcohol species significantly alter the physicochemical properties at the hematite/TiO_2 interface and in bulk hematite. These changes are primarily manifested in the modulation of the density of states and resistance to promote the charge carrier transport. For example, ethanol and butanol were found to enhance the electron density of states at the interface, which correlates with higher photocurrent outputs and improved PEC activity. In contrast, methanol showed a less pronounced effect, suggesting a nuanced interaction between the alcohol molecular structure and hematite surface chemistry. These findings not only underscore the importance of tailored precursor solution chemistry for enhancing PEC performance but also highlight the power of ML tools in uncovering the underlying physical and chemical mechanisms that govern the behavior of complex material systems. This study sets a foundational approach where ML can bridge the gap between empirical observations and theoretical understanding, leading to the rational design of energy materials.

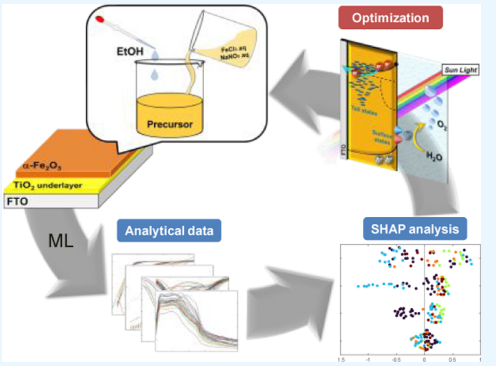

INTRODUCTION

Hematite (α-Fe_2O_3) stands out as a highly favored material for photoanode applications, thanks to its widespread availability as a natural resource and its cost-efficiency.[1] It is easily recognizable by its rust-like orange color, indicating its ability to absorb visible light. This absorption capacity is due to its bandgap, which is roughly 600 nm (2.1 eV), making it an excellent option for photocatalytic activities that utilize visible light. However, the effectiveness of hematite is hindered by several issues: its low absorption coefficient, poor conductivity for the majority of carriers, and the short diffusion length of minority carriers (less than 4 nm), which is further aggravated by a significant overpotential.[2] In an effort to overcome these drawbacks, there has been a concentrated effort on improving the material through various strategies such as doping, passivation, and enhancing crystal growth.[3−7] Despite these efforts, a consistent challenge remains in the reproducible preparation of hematite,[5,8] an issue we have previously analyzed and attempted to solve by investigating techniques to improve reproducibility.[8,9]

We have created a method that successfully pinpoints the key physical and chemical influences on the performance of photoelectrochemical (PEC) systems. This technique marries machine learning (ML) with an extensive collection of analytical data. Generally, employing ML to optimize materials science requires a data set with more than a thousand samples, often derived from existing databases[10,11] or produced through high-throughput experimental methods.[12,13] Yet, gathering such large data sets can be difficult for materials that have not been extensively studied. To address this issue, we integrated a wide array of analytical data to provide detailed insights into the materials being examined. By leveraging this data, we are able to represent materials in a way that facilitates the creation of an ML model capable of predicting PEC performance with a data set that includes only a few dozen

Received: September 20, 2024
Accepted: October 14, 2024
Published: October 24, 2024

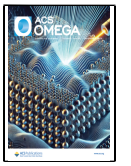

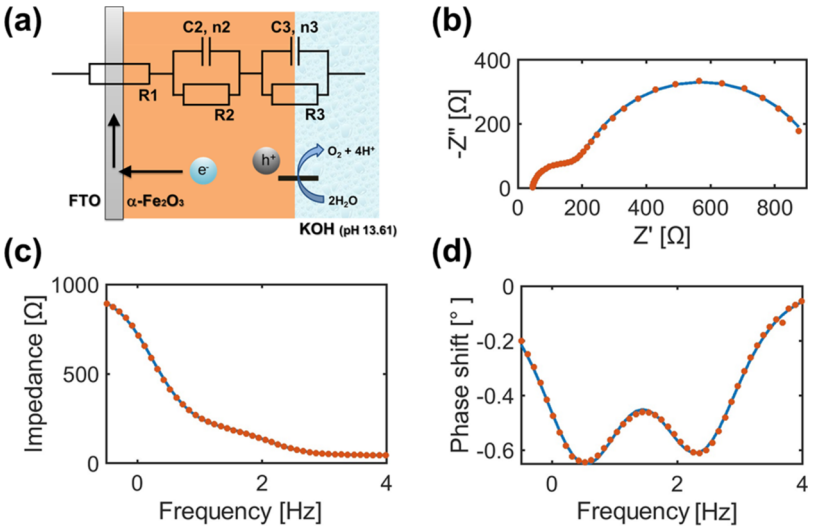

Figure 1. Analysis of photoelectrochemical impedance spectra (PEIS) with a circuit model. The capacitor is modeled with a constant phase element (CPE). (a) The equivalent circuit for a hematite photoanode, (b) Nyquist plot, and (c, d) Bode plots for impedance and phase are shown with fitting curves.

instances,[8] and this methodology has been recently completed in a robust manner.[14]

Prior research has shown that the PEC performance of hematite samples can vary widely, even when they are prepared in the same way. This variation was attributed to specific characteristics identified in the analytical data.[8,15] Additionally, it was found that some samples of hematite did not display any photoelectrode activity at all. By applying a classification technique that uses ML, we could identify these inactive samples and pinpoint the exact reasons for their lack of activity.[9] One critical issue discovered was the high resistivity at the hematite/fluorine-doped tin oxide (FTO) interface. To overcome this problem, we introduced a TiO_2 underlayer between the hematite and the FTO substrate, which successfully resolved the inactivity issue, ensuring that all modified films reached a minimum activity level of 0.05 mA/cm^2. Moreover, adding the TiO_2 underlayer not only improved the interface transfer but also enhanced the hematite's overall bulk and surface characteristics, resulting in a notable enhancement of its PEC performance.

The introduction of a TiO_2 underlayer effectively resolved the issue of generating inactive samples and substantially improved the overall performance.[16] However, we noticed that the variety in the photocurrent density was still large. In an effort to tackle the challenge of achieving consistent results, we found that the precursor solutions including ethanol[17] greatly improve the reproducibility, and also this improvement was observed specifically in samples prepared with a TiO_2 underlayer. The detailed mechanism was studied with bias-dependent photoelectrochemical impedance spectroscopy (PEIS), which was used for studying the surface states based on band diagram for hematite,[18−20] to clarify the photo-generated electron transport in the bulk and the photo-generated hole transfer at the interface based on the band structure.[16]

However, the effect of alcohol and its combination with the underlayer is still not clear, although the contributions of electrons and holes have been clarified. In this study, we developed a new ML scheme recently developed[14] to clarify the effect of the underlayer and the alcohol deposition using the SHapley Additive exPlanations (SHAP) diagram obtained from the ML calculation, and furthermore, this study indicates the dominant cause for the photoelectrochemical (PEC) performance (photocurrent, turn-on voltage, etc.) and its relation with the experimental parameters, alcohol species. This is a new methodology to link the experimental operation parameters to the performance, with analytical data as a connecting information.

METHODS

We prepared four different types of hematite electrodes using a straightforward manufacturing technique.[21] For the production of bare hematite on FTO, we applied the solution deposition approach. The starting solution was made by dissolving iron(III) chloride hexahydrate (3.04 g, 99.9%, Wako) and sodium nitrate (6.38 g, 99.9%, Wako) in deionized water (75 mL), which was then used as an immersion solution for a cleaned FTO substrate (∼7 Ω sq^{-1}, SOLARONIX) after washing it with water and ethanol. The substrate was submerged in this solution and heated to 100 °C in an oil bath. This process led to a reaction between the two chemicals, resulting in the deposition of β-FeOOH on the FTO surface for 3 h as the solution turned cloudy. Once the mixture was cooled to ambient temperature, the substrate was washed with deionized water. The β-FeOOH/FTO underwent calcination at 700 °C for 30 min in an electric furnace, heating at a rate of 5 °C/min, to form hematite photoanodes. A short calcination period was chosen to minimize the degradation of the FTO.

In instances where a TiO_2 underlayer was introduced between the FTO and hematite layers, a titanium-based precursor solution, specifically 0.15 M titanium diisopropoxide bis(acetylacetonate) (75 wt % in isopropanol, Aldrich) mixed in 1-butanol, was applied onto the FTO substrate using spin-coating (1500 rpm for 30 s) and subsequently heated at 250 °C for 30 min.[22,23] The process for depositing hematite on top was identical to the one described in the previous paragraph. Through these steps, we successfully created hematite electrodes with a TiO_2 underlayer on FTO substrates.

For the creation of hematite electrodes deposited in an aqueous alcohol solution on a TiO_2/FTO substrate (hematite-

https://doi.org/10.1021/acsomega.4c08633
ACS Omega 2024, 9, 44837−44845

alcohol/TiO_2/FTO), we followed the same procedure for the preparation of the TiO_2 underlayer. However, when preparing the precursor layer (β-FeOOH), we used a solution mixed with 10% alcohol by volume. To evaluate the combined impact of TiO_2 and alcohol, we also synthesized hematite-alcohol/FTO (where hematite was deposited with alcohol but without a TiO_2 underlayer) following the same method used for bare hematite/FTO, but with 10% alcohol incorporated into the solution. The concentration was optimized to enhance the reproducibility of the PEC performance, but the effect of the concentration was minor for 2.5−15%. The used alcohols were methanol (MeOH), ethanol (EtOH), butanol (BuOH), and 2-ethyl-1-butanol (EBOH).

The efficiency of photoanodes was assessed using potential−current (J−V) curves within a PEC cell under illumination from a solar simulator (AM1.5 G). The PEC cell was configured with a three-electrode system submerged in a potassium hydroxide (1 M, pH = 13.61) solution, where the counter and reference electrodes were a platinum wire and Ag/AgCl electrode, respectively. We controlled the working electrode's potential via a potentiostat (SI1287, Solartron) at a scan rate of 20 mV/s, ranging from −0.5 to 0.5 V (vs Ag/AgCl).

Additionally, we conducted analyses through photoelectrochemical impedance spectroscopy (PEIS) using instruments (Models 660A, BAS, and 1260A, Solartron). For the PEIS tests, we examined the electrodes at a potential 1.0 V vs RHE with an alternating current (AC) voltage amplitude of 5 mV across a frequency spectrum of 0.1 to 10,000 Hz.

The analysis of the PEIS data for the hematite photoanode was performed using a standard modeling technique, same as previously.[16] This approach treats the photoanode as a network of capacitors and resistors arranged in parallel, corresponding to three specific regions: the interface between hematite and FTO, the bulk of hematite, and the interface with the electrolyte, as illustrated in Figure 1. Instead of a simple capacitor model ($Z = 1/(i\omega C)$), a constant phase element (CPE) model ($Z = 1/(i\omega C)^n$) was utilized. The CPE model accounts for the frequency-dependent behavior of the capacitance, including the effects of carrier leakage influenced by the rate of charge transfer. Here, the parameter "n" is adjusted to reflect deviations from the ideal capacitor behavior. One of the example data and fitting curves are shown in Figure 1, including the Nyquist plot and Bode plots that show the real and imaginary components of the impedance, along with the fitting curves. These fitting curves were continuously refined through iterative calculations until the difference between the model predictions and the actual experimental observations fell within a preset error margin. The circuit resistance (R_1), the bulk resistance (R_2) and capacitance (C_2), and the interfacial resistance (R_3) and capacitance (C_3) were obtained as descriptors in this analysis. As another analysis, X-ray diffraction (XRD) (Ultima IV, Rigaku) was performed in the range of 10−60° in 0.01° steps. A typical XRD pattern is shown in Figure 2, indicating the peaks and positions used for the descriptors, and the explanation for these peaks' assignment is provided in Figure S2.

Our ML calculation scheme is described here, which is summarized in a flowchart in Figure S2. The dominant features for predicting the target values were selected through a three-step feature selection method, developed and elaborated in our previous study.[14] All of the features were normalized for fair comparison, and the relative standard deviation (RSD) was

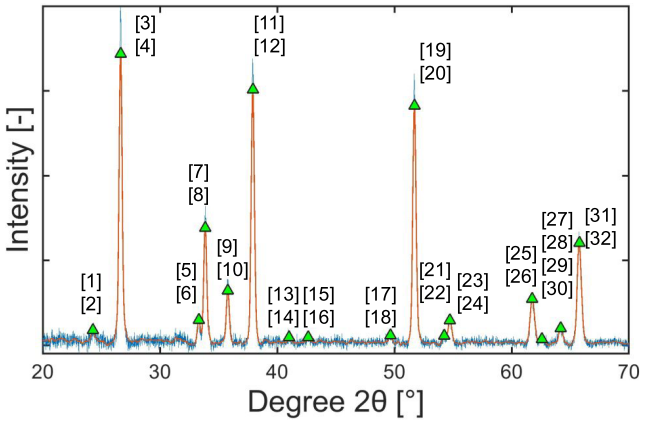

Figure 2. Example of an XRD pattern of a Fe_2O_3 photoanode shown with a descriptor indication. The peak intensities and positions were used as features. The assignments for these features are shown in Figure S1.

calculated for each of the features. The features with small variations (low RSD) were removed from the data set because they were almost constant regardless of the sample property difference. The relative correlation coefficients between the remaining features were calculated to group the features with high absolute correlation coefficients into clusters to reduce both multicollinearity and dimensionality. The features and clusters were sequentially added to each one of the nonlinear models to predict the target. The models included support vector regression (SVR), Gaussian process regression (GPR), decision tree (DT), and ensemble models. The original data set was split into two: the training data set (80%) and the test data set (20%). A 5-fold cross-validation was applied to the model to reduce the overfitting of the training data sets. The prediction accuracy of the model was evaluated by the coefficient of determination (R^2), and the combination of features and clusters that generate the highest R^2 value of the test data set were selected as the dominant features.

The Shapley plots were drawn based on the SHAP analysis results.[24,25] The selected features were ranked based on their importance to the prediction of the target for revealing the underlying relationships between these features and the target and for understanding their chemical or physical meaning. We used two different types of SHAP plots. One is the one originally used; the Shapley values of individual sample data points in each corresponding feature. The color gradients demonstrate trends between the features and the target. The other is the newly created; each Shapley values of individual data points are colored differently by the experimental operation (in this case, alcohol species), referred to as "operational SHAP plot." here.

RESULTS AND DISCUSSION

Effect of the TiO_2 Underlayer. We first studied the effect of the TiO_2 underlayer. We prepared bare hematite with and without a TiO_2 underlayer. We had 61 bare hematite and 41 hematite with a TiO_2 underlayer, in total 102 samples. The photocurrent−applied voltage (I−V) curves for all of the samples are shown in Figure 3. From this figure, the photocurrent at 1.23 V vs RHE had a large variation, and the photocurrent values were predicted by the descriptors obtained from the analytical data: XRD patterns and PEIS. The

https://doi.org/10.1021/acsomega.4c08633
ACS Omega 2024, 9, 44837−44845

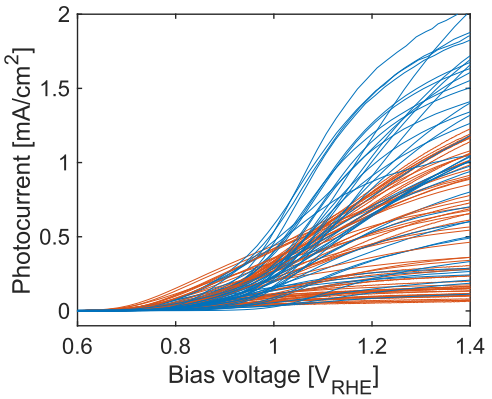

Figure 3. Current density−voltage curves were measured by linear sweep voltammetry for 102 samples of hematite photoanodes, and they were displayed. The samples include hematite films prepared with (41, blue) and without (61, red) a TiO_2 underlayer. The precursor solutions were pure aqueous solutions.

analyzed PEIS data (R_1−R_3, C_2, C_3, n_2, n_3) are tabulated in Table S1 in the SI.

The response plots for the training and test data sets are shown in Figure 4. The determination coefficients (R^2) of the training and test data sets were 0.989 and 0.878, and they were sufficiently high for the experimental data sets. The dominant descriptors and the corresponding SHAP plots are listed in Figure 5(a,b). The dominant descriptors for the performance of this data set are cluster 5 (resistance combination of R_2 and R_3, the 15th peak of XRD), cluster 4 (capacitance and its adjusting parameter combination for the bulk hematite), and cluster 2 (combination of XRD peak combinations).

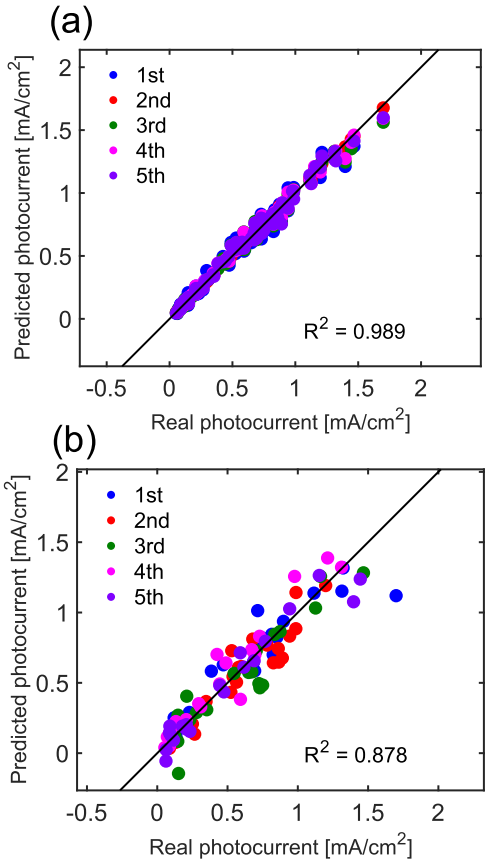

Figure 4. Prediction results of the photocurrent density are shown for (a) the training data set and (b) the test data set, and the determination coefficients (R^2) were 0.989 and 0.878, respectively. The color difference of the plots indicated different data sets of the 5-fold cross-validation for hematite The samples include hematite films prepared with (41) and without (61) TiO_2 underlayer. The precursor solutions were pure aqueous solutions.

It is understood that the PEC performance is largely determined by the resistances in the bulk and at the solution interface, and they had a negative impact on the performance, meaning that the lower the better. It is quite reasonable because it indicates that smaller resistances are better for performance. The 15th peak of the XRD corresponds to the hematite facet of (300). Several reports indicate the active surfaces of hematite, and mostly {104}, {100}, and {001} facets are often referred. The (300) surface belongs to the group of {100}, and possibly one of the active surfaces.[26−29] In this data set, {104}, often referred to as an active facet, was not selected; this does not indicate the facet was inactive but the facet was not used for differentiating the samples constructed in the ML function. The capacitance descriptor in the bulk corresponds to the shallow states near the conduction bands, which are used for electron transport. The final cluster 2 consisting of XRD peaks provided a minor contribution compared to the other descriptors.

The operation SHAP, which is a plot representing the SHAP values colored by the experimental operations, is shown in Figure 5(c). The dominance was clearly observed with and without the TiO_2 underlayer in the third descriptor, Cluster 4. The no-TiO_2 provides a negative impact on the PEC performance, while the TiO_2 underlayer provides a broad range of impacts on the PEC performance, mostly in the positive effect. The C_2 value corresponds to the density of state (DOS) of the majority carriers, electrons in the bulk hematite.[30] The result indicates that the larger the DOS, the performance is better, because this DOS corresponds to the shallow trap states of electrons, used for the electron transport,[16] and it is better to have a larger density of DOS for it. There is a possibility that Ti ions may migrate and are doped in hematite during the calcination process.[31−33] It is known that Ti-doped hematite has a higher photocatalytic activity. An increase in the shallow states could be attributed to the doping effect.

There is also some systematic difference in Cluster 2, and the crystal surfaces were also affected by the TiO_2 underlayer. In short, the TiO_2 underlayer, which was intended to reduce the resistance between the FTO and hematite, had an influence on the growth of hematite, increasing the shallow trap states in the bulk; concurrently, the crystal facets were modified. This demonstration could clearly show that the experimental operational parameter distinction in the dominant descriptors in SHAP plots could pinpoint the dominant origin of the physical parameters affecting the target by the experimental operation. In this strategy, it is important to mix the samples with different experimental operations to differentiate which dominant descriptors are affected by the experimental operation. If the operation affects one of them, the SHAP values will be differentiated by the experimental operation.

Effect of Alcohol for the Deposition. In the previous study,[34] the variation of the PEC performance was suppressed when EtOH was added 10% in the precursor solution during the deposition, and this effect was only valid when the TiO_2

https://doi.org/10.1021/acsomega.4c08633
ACS Omega 2024, 9, 44837−44845

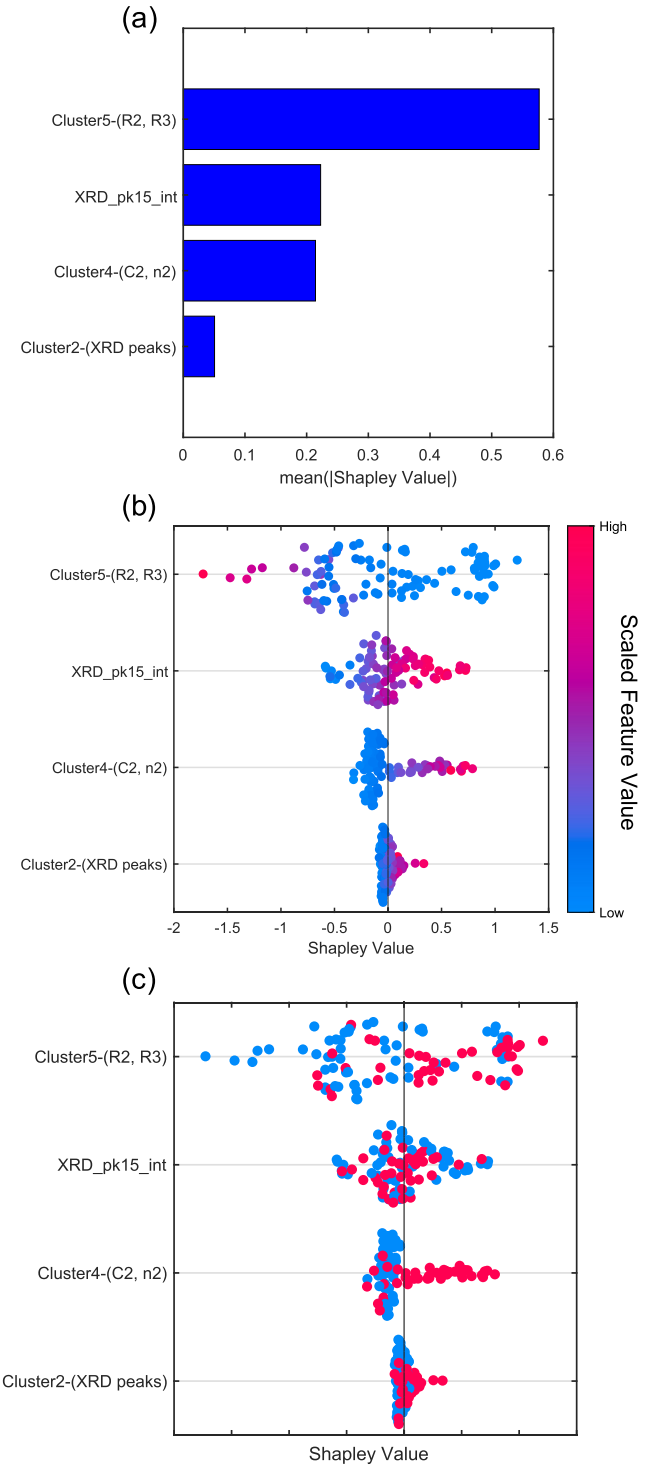

Figure 5. (a) Contributions of the selected dominant descriptor shown by the mean absolute Shapley values. (b) Scatter plot illustrating samples' Shapley values for each feature. (c) Same plot as (b), but blue and red plots correspond for the samples without and with TiO_2 underlayer, respectively. The samples include hematite films prepared with and without a TiO_2 underlayer (41 and 61 samples). The precursor solutions were pure aqueous solutions. Cluster 2 corresponds to the XRD peaks of (peak 1st, 3rd, 7th, 9th, and 11th intensities).

underlayer was used. In this section, we studied the effect of alcohol included in the precursor solutions. The data include the XRD and PEIS data for the precursor solution including different alcohol species, MeOH (15 samples), EtOH (9 samples), BuOH (9 samples), and EBOH (6 samples), and also include the one without an alcohol with and without the TiO_2 underlayer (9 and 12 samples, respectively), in total 60 samples. It is reminded that including the different types of experimental conditions makes the distinction of the effects on the dominant descriptors clear.

The IV curves for these samples are shown in Figure 6. It is noted that there are almost no inactive photoanodes (<0.05

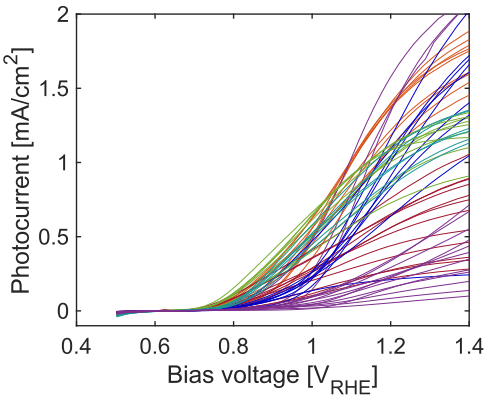

Figure 6. Current density−voltage curves measured by linear sweep voltammetry for 60 samples of hematite photoanodes. The samples include hematite films prepared under various conditions: hematite without TiO_2 underlayer (12 samples, dark red), hematite with TiO_2 underlayer prepared in an aqueous precursor solution (9 samples, dark blue), and hematite with TiO_2 underlayer prepared in aqueous precursor solutions including 10% methanol (15 samples, purple), ethanol (9 samples, red), butanol (9 samples, green), and 2-ethyl-1-butanol (6 samples, cyan).

mA/cm^2) in this data set, because of the effect of the TiO_2 underlayer.[9] Using the XRD and PEIS data (the analyzed PEIS parameters are shown in Table S2 in the SI), the photocurrents at 1.23 V (vs RHE) were predicted for 61 samples, and the response plots for the training and test data sets are shown in Figure 7. The R^2 values for the training and test data sets were 1.00 and 0.954, which were considerably high for the experimental data sets of photoanodes and well predicted.

The selected dominant descriptors were resistance descriptors (R_1, R_2, R_3) and the cluster descriptor consisted of XRD peaks (Figure 8). The PEC performance was dominated by the resistance descriptors, and all of them provide a negative correlation with the PEC performance, indicating that the photocurrent is larger as they are smaller, which is quite reasonable and does not provide much information.

However, the dominant descriptor distribution for different alcohol species in the precursor solutions provides much information on what kinds of modifications were given by changing the alcohol solutions (Figure 8(c)). The R_2, the bulk resistance, distributed uniformly in the positive and negative contributions in the PEC performance in case that aqueous solutions without alcohol was used as precursor solutions. However, when alcohol species are included in the precursor solutions, the R_2 values were distributed depending on the alcohol species. MeOH provided the most negative effect, while EtOH gave a positive effect, and the longer alcohol provided a medium impact on the PEC performance. The R_3 values are further divided by the included alcohol species clearly. From the positive impact side, ethanol, BuOH, and

https://doi.org/10.1021/acsomega.4c08633
ACS Omega 2024, 9, 44837−44845

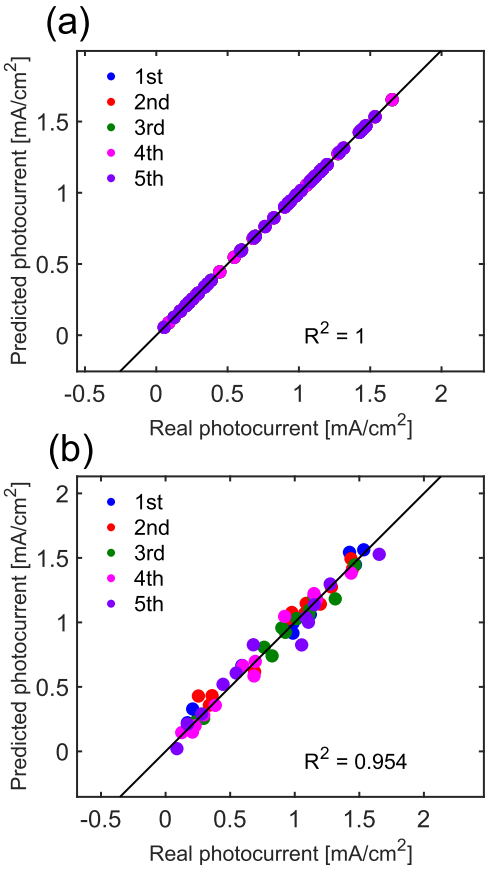

Figure 7. Prediction results of the photocurrent density are shown for (a) the training data set, and (b) the test data set, and the determination coefficients (R^2) were 1.00 and 0.954, respectively. The color difference of the plots indicated different data sets of the 5-fold cross-validation for hematite The samples include hematite films prepared under various conditions: hematite without TiO_2 underlayer (12 samples), hematite with TiO_2 underlayer prepared in an aqueous precursor solution (9 samples), and hematite with TiO_2 underlayer prepared in aqueous precursor solutions including 10% methanol (15 samples), ethanol (9 samples), butanol (9 samples), and 2-ethyl-1-butanol (6 samples).

EBOH were aligned as a positive impact for the PEC performance, and MeOH clearly provides a negative impact and water influences positively and negatively. It is clear that the deposition solution could affect the hole transfer at the interface. With regard to the R_1 values, they were clearly separated if the precursor solutions include alcohol or not. Alcohol inclusion in the precursor solutions provided a positive effect regardless of the alcohol species. Since cluster 2 consisting of various XRD peaks showed no clear dependence on the alcohol species; there seems no indication of the facet control with alcohol species.

In short, the alcohol inclusion clearly makes a better contact with hematite on the TiO_2 underlayer, possibly due to the support of the hydrogen bonding on the TiO_2 surface to the hematite growth. The shallow states (defect states) included in hematite were modified with the alcohol species included, affecting the R_2 values. Also it affects the hole transfer at the interface due to the final surface morphology. It seems that the alcohol species could modify the crystal growth processes; as a result, the defect states and the final interface could be controlled for optimization of charge transport.

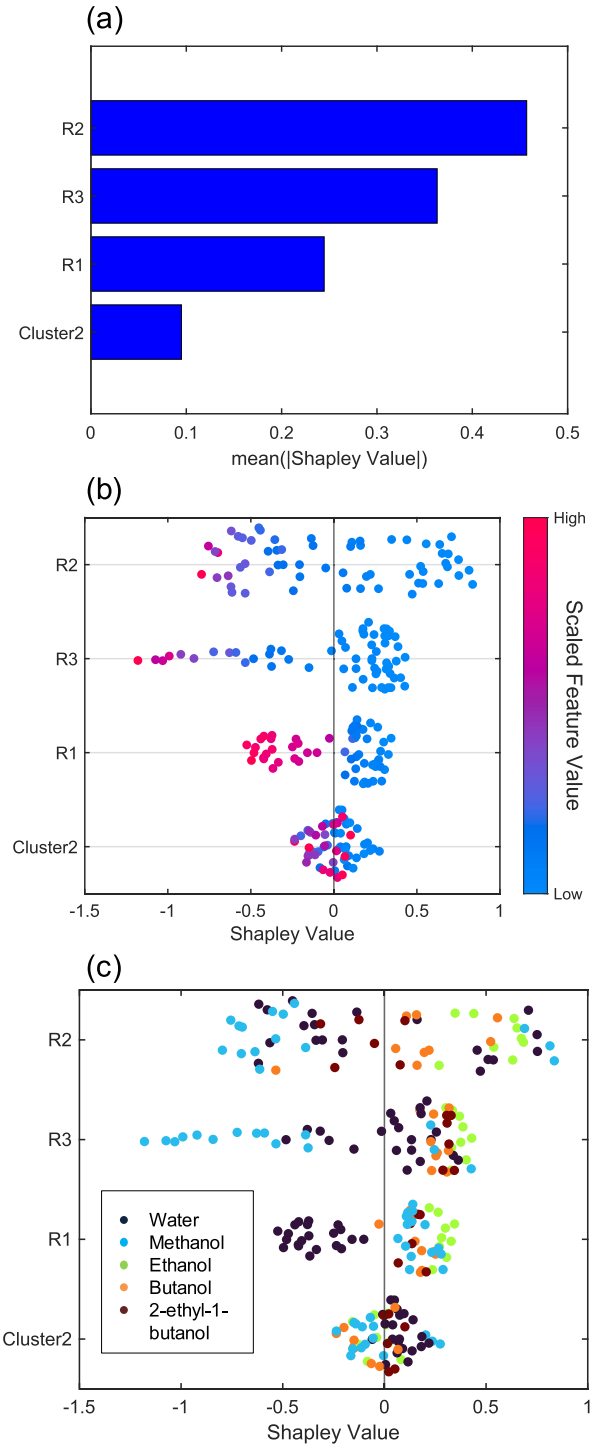

Figure 8. (a) Contributions of the selected dominant descriptor are shown by the mean absolute Shapley values. (b) Scatter plot illustrating samples' Shapley values for each feature is displayed. (c) Scatter plot illustrating samples' Shapley values for each feature displayed with different colors for the precursor solution types. The samples include hematite films prepared under various conditions: hematite without TiO_2 underlayer (12 samples), hematite with TiO_2 underlayer prepared in an aqueous precursor solution (9 samples), and hematite with TiO_2 underlayer prepared in aqueous precursor solutions including 10% methanol (15 samples), ethanol (9 samples), butanol (9 samples), and 2-ethyl-1-butanol (6 samples).

Effect of Alcohol for the Onset Potential. This ML strategy can be used for not only predicting the photocurrent

https://doi.org/10.1021/acsomega.4c08633
ACS Omega 2024, 9, 44837−44845

but also any sort of performance. One of the important parameters in the PEC performance is the onset potential, where the photocurrent starts to increase. The position of the photocurrent increase is important when the overall water splitting is considered by a combination of the photoanode and the photocathode.

The onset potentials from Figure 6 were obtained by identifying the intersection point where the linear part of the photocurrent curve overlapped with the baseline. The potential was predicted using the same descriptors obtained from the XRD and PEIS descriptors. The prediction results are shown in Figure 9 for the training and test data sets. The R_2 values were

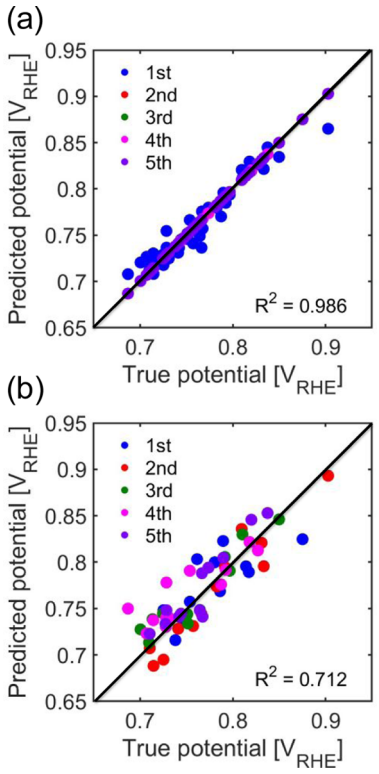

Figure 9. Prediction results of the turn-on voltage are shown for (a) the training data set and (b) the test data set, and the determination coefficients (R^2) were 0.986 and 0.712, respectively. The color difference of the plots indicated different data sets of the 5-fold cross-validation for hematite The samples include hematite films prepared under various conditions: hematite without TiO_2 underlayer (12 samples), hematite with TiO_2 underlayer prepared in an aqueous precursor solution (9 samples), and hematite with TiO_2 underlayer prepared in aqueous precursor solutions including 10% methanol (15 samples), ethanol (9 samples), butanol (9 samples), and 2-ethyl-1-butanol (6 samples).

0.986 and 0.712, respectively. The test result was not as good as the results for photocurrent values, but it could ensure a certain level of prediction of the onset potential.

The SHAP results are shown in Figure 10. Even though the same analytical data and PEC performance were used in the previous example, the selected dominant descriptors were different from the ones selected in Figure 8. The selected descriptors were capacitor descriptors (C_2 and C_3), including R_2 as the third dominant descriptor. The difference between the descriptors in Figures 8 and 10 indicates that the dominant physical origins were different for the photocurrent and the onset potential. The selection of C_3 clearly indicates that the

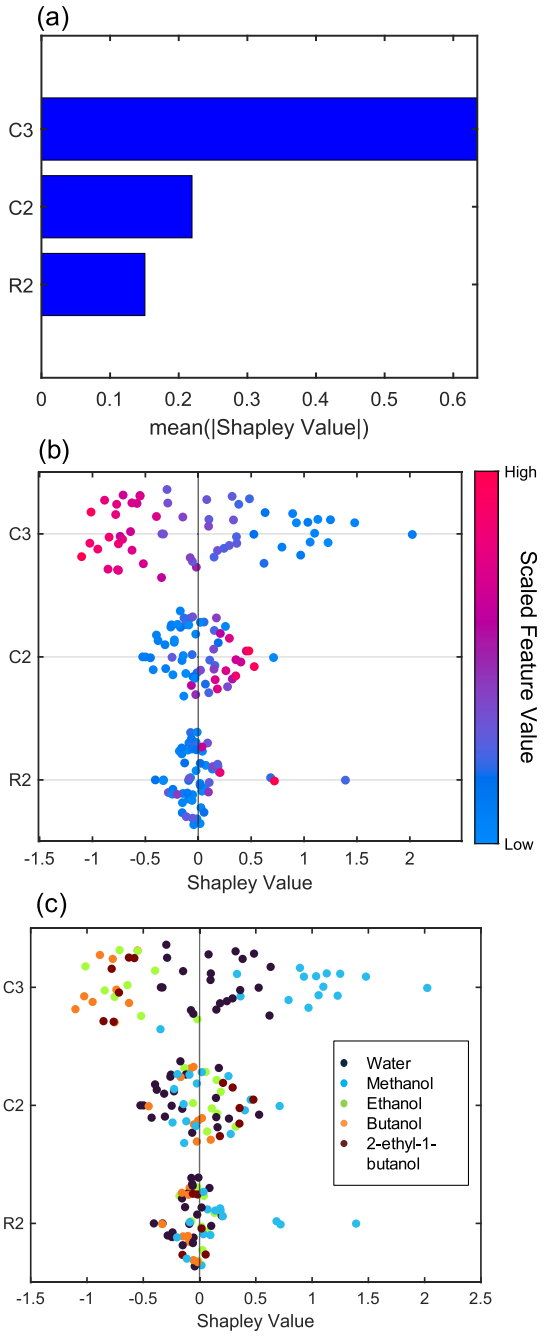

Figure 10. (a) Contributions of the selected dominant descriptor for prediction of the turn-on voltage shown by the mean absolute Shapley values. (b) Scatter plot illustrating samples' Shapley values for each feature. (c) Scatter plot illustrating samples' Shapley values for each feature displayed with different colors for the precursor solution types. The samples include hematite films prepared under various conditions: hematite without TiO_2 underlayer (12 samples), hematite with TiO_2 underlayer prepared in an aqueous precursor solution (9 samples), and hematite with TiO_2 underlayer prepared in aqueous precursor solutions including 10% methanol (15 samples), ethanol (9 samples), butanol (9 samples), and 2-ethyl-1-butanol (6 samples).

density of states at the solution interface is important for the onset potential, indicating that it affects the overpotential. Not only the C_3 but also the C_2 were important for the onset potential because C_2 corresponds to the shallow (defect) states and could change the Fermi level control when the bias potential is applied.

https://doi.org/10.1021/acsomega.4c08633
ACS Omega 2024, 9, 44837−44845

Looking at the operational SHAP plot for different alcohol species (Figure 10), only C3 was clearly separated by the alcohol species. Since the turn-on voltage is better for smaller values, and the negative SHAP values are preferred. The SHAP values were lower for BuOH, EBOH, and EtOH, while methanol provides a larger turn-on voltage. Water provides a medium effect on it. The operation-colored SHAP graph indicated clearly that the C3 was mainly controlled by the alcohol species included in the precursor solutions, and this leads to the conclusion that the onset potential is mainly controlled by the solution interfaces and can be controlled by the alcohol species in the precursor solutions.

CONCLUSIONS

This research follows the previous finding that the TiO_2 underlayer can remove the inactivity of the hematite photoanodes and the PEC performance reproduction is improved when the precursor solution contains ethanol. To study the effect of alcohol including ethanol with a TiO_2 underlayer, we incorporated the machine learning (ML) strategy and SHapley Additive exPlanations (SHAP) analysis for the selected dominant descriptors selected from the analytical data of the photoanodes.

The detailed mechanistic insights provided by our ML analysis, particularly through SHAP, have elucidated the impact of the dominant descriptors selected from the analytical data on the PEC properties. The dominant factors identified were the resistance, the density of state modifications in the hematite layer, further elucidated by the connection between the SHAP values with the experimental operations, namely, the alcohol species. The connection between the SHAP values and the experimental operation was able to modify and optimize the PEC performance. The effect of alcohol species was reflected in changes to the density of states and interfacial capacitance, which, in turn, affected the electron and hole dynamics critically involved in the PEC process. This detailed understanding allowed us to fine-tune the deposition process to achieve the desired photoelectrochemical properties more reliably.

Looking toward the future, this work opens several promising avenues for further research. First, the exploration of other alcohols and their concentrations in the precursor solutions may provide additional ways to tune the material properties and enhance the PEC performance. Each type of alcohol may interact differently with the hematite and TiO_2 surfaces, potentially leading to new insights into the growth mechanisms and interface dynamics.

Additionally, integrating other theoretical calculations with experimental approaches could yield a deeper understanding and more precise control over the material characteristics. For instance, advanced simulation methods could be employed to predict and visualize the interactions at the interfaces, thereby guiding the optimization of the deposition processes.

ASSOCIATED CONTENT

Data Availability Statement

All of the source analytical data and the codes for the descriptor selection and the performance prediction are available in GitHub (https://github.com/Katayama-ChuoU/PhotocatML).

Supporting Information

The Supporting Information is available free of charge at https://pubs.acs.org/doi/10.1021/acsomega.4c08633.

XRD pattern of hematite and the assignment of peaks (Figure S1); and our machine learning scheme for the determination of dominant descriptors (Figure S2); and electrical parameters obtained from PEIS for hematite w/wo TiO_2 underlayer data (Table S1); and electrical parameters obtained from PEIS for hematite prepred in various aqueous solutions including different alcohol species (Table S2) (PDF)

AUTHOR INFORMATION

Corresponding Author

Kenji Katayama − *Department of Applied Chemistry, Chuo University, Tokyo 112-8551, Japan;* orcid.org/0000-0003-3278-6485; Phone: +81-3-3817-1913; Email: kkata@kc.chuo-u.ac.jp

Authors

Takumi Idei − *Department of Applied Chemistry, Chuo University, Tokyo 112-8551, Japan*

Yuya Nagai − *Department of Applied Chemistry, Chuo University, Tokyo 112-8551, Japan*

Zhenhua Pan − *Department of Applied Chemistry, Chuo University, Tokyo 112-8551, Japan;* orcid.org/0000-0001-9838-7685

Complete contact information is available at: https://pubs.acs.org/10.1021/acsomega.4c08633

Author Contributions

T.I. performed the experiments and analyses, Y.N. supported the SHAP analyses, Z.P. supported the PEIS measurements, and K.K. guided the overall research. T.I. and K.K. wrote the manuscript, and all of the authors reviewed it.

Notes

The authors declare no competing financial interest.

ACKNOWLEDGMENTS

The research was financially supported by JSPS Kakenhi (#22K05158), Iketani Science and Technology Foundation, and the Institute of Science and Engineering, Chuo University.

REFERENCES

(1) Wang, Q.; Domen, K. Particulate Photocatalysts for Light-Driven Water Splitting: Mechanisms, Challenges, and Design Strategies. *Chem. Rev.* **2020**, *120* (2), 919−985.

(2) Li, J.; Chen, H.; Triana, C. A.; Patzke, G. R. Hematite Photoanodes for Water Oxidation - Electronic Transitions, Carrier Dynamics, and Surface Energetics. *Angew. Chem., Int. Ed.* **2021**, *60*, 18380−18396, DOI: 10.1002/anie.202101783.

(3) Wheeler, D. A.; Wang, G.; Ling, Y.; Li, Y.; Zhang, J. Z. Nanostructured Hematite: Synthesis, Characterization, Charge Carrier Dynamics, and Photoelectrochemical Properties. *Energy Environ. Sci.* **2012**, *5* (5), 6682−6702.

(4) He, Y.; Hamann, T.; Wang, D. Thin Film Photoelectrodes for Solar Water Splitting. *Chem. Soc. Rev.* **2019**, *48*, 2182−2215.

(5) Phuan, Y. W.; Ong, W.-J.; Chong, M. N.; Ocon, J. D. Prospects of Electrochemically Synthesized Hematite Photoanodes for Photoelectrochemical Water Splitting: A Review. *J. Photochem. Photobiol., C* **2017**, *33*, 54−82.

(6) Shen, S.; Lindley, S. A.; Chen, X.; Zhang, J. Z. Hematite Heterostructures for Photoelectrochemical Water Splitting: Rational

Materials Design and Charge Carrier Dynamics. *Energy Environ. Sci.* **2016**, *9* (9), 2744−2775.
(7) Bedin, K. C.; Muche, D. N. F.; Melo, M. A., Jr.; Freitas, A. L. M.; Gonçalves, R. V.; Souza, F. L. Role of Cocatalysts on Hematite Photoanodes in Photoelectrocatalytic Water Splitting: Challenges and Future Perspectives. *ChemCatChem* **2020**, *12* (12), 3156−3169.
(8) Nagai, Y.; Katayama, K. Prediction of the Photoelectrochemical Performance of Hematite Electrodes Using Analytical Data. *Analyst* **2022**, *147* (7), 1313−1320.
(9) Idei, T.; Nagai, Y.; Pan, Z.; Katayama, K. Identification of the Contributing Factors to the Photoelectric Conversion Efficiency for Hematite Photoanodes by Using Machine Learning. *ACS Appl. Mater. Interfaces* **2023**, *15* (48), 55644−55651.
(10) Mai, H.; Le, T. C.; Chen, D.; Winkler, D. A.; Caruso, R. A. Machine Learning for Electrocatalyst and Photocatalyst Design and Discovery. *Chem. Rev.* **2022**, *122* (16), 13478−13515.
(11) Liu, Y.; Guo, B.; Zou, X.; Li, Y.; Shi, S. Machine Learning Assisted Materials Design and Discovery for Rechargeable Batteries. *Energy Storage Mater.* **2020**, *31*, 434−450.
(12) Recatala-Gomez, J.; Suwardi, A.; Nandhakumar, I.; Abutaha, A.; Hippalgaonkar, K. Toward Accelerated Thermoelectric Materials and Process Discovery. *ACS Appl. Energy Mater.* **2020**, *3* (3), 2240−2257.
(13) Yang, K.; Xu, X.; Yang, B.; Cook, B.; Ramos, H.; Krishnan, N. M. A.; Smedskjaer, M. M.; Hoover, C.; Bauchy, M. Predicting the Young's Modulus of Silicate Glasses Using High-Throughput Molecular Dynamics Simulations and Machine Learning. *Sci. Rep.* **2019**, *9* (1), No. 8739.
(14) Tajima, M.; Nagai, Y.; Chen, S.; Pan, Z.; Katayama, K. Robust Methodology for PEC Performance Analysis of Photoanodes Using Machine Learning and Analytical Data. *Analyst* **2024**, *149*, 4193−4207, DOI: 10.1039/d4an00439f.
(15) Kobayashi, K.; Nagai, Y.; Pan, Z.; Katayama, K. Identification of Dominant Factors Contributing to Photocurrent Density of BiVO4 Photoanodes Using Machine Learning. *J. Photochem. Photobiol., A* **2023**, *440*, No. 114651.
(16) Idei, T.; Pan, Z.; Katayama, K. Combined Effect of Underlayer and Deposition Solution to Optimize the Alignment of Hematite Photoanodes. *Langmuir* **2024**, *40* (22), 11526−11533.
(17) Chen, Y.-J.; Okazaki, M.; Furube, A.; Chen, L.-Y. Ultrafast Timescale Charge Carrier Dynamics in Nanocomposite Hematite Photoelectrodes. *J. Photochem. Photobiol., A* **2023**, *442*, No. 114820.
(18) Klahr, B.; Hamann, T. Water Oxidation on Hematite Photoelectrodes: Insight into the Nature of Surface States through In Situ Spectroelectrochemistry. *J. Phys. Chem. C* **2014**, *118* (19), 10393−10399.
(19) Klahr, B.; Gimenez, S.; Fabregat-Santiago, F.; Bisquert, J.; Hamann, T. W. Photoelectrochemical and Impedance Spectroscopic Investigation of Water Oxidation with "Co−Pi"-Coated Hematite Electrodes. *J. Am. Chem. Soc.* **2012**, *134* (40), 16693−16700.
(20) Pan, Z.; Chen, S.; Katayama, K. Roles of Surface States in Cocatalyst-Loaded Hematite Photoanodes for Water Oxidation. *J. Phys. Chem. C* **2023**, *127* (7), 3904−3909.
(21) Kim, J. Y.; Youn, D. H.; Kang, K.; Lee, J. S. Highly Conformal Deposition of an Ultrathin FeOOH Layer on a Hematite Nanostructure for Efficient Solar Water Splitting. *Angew. Chem., Int. Ed.* **2016**, *55* (36), 10854−10858.
(22) Park, J. W.; Mahadik, M. A.; Ma, H.; An, G. W.; Lee, H. H.; Choi, S. H.; Chae, W.-S.; Chung, H.-S.; Jang, J. S. Improved Interfacial Charge Transfer Dynamics and Onset Shift in Nanostructured Hematite Photoanodes via Efficient Ti4+/Sn4+ Heterogeneous Self-Doping Through Controlled TiO2 Underlayers. *ACS Sustainable Chem. Eng.* **2019**, *7* (7), 6947−6958.
(23) Hisatomi, T.; Dotan, H.; Stefik, M.; Sivula, K.; Rothschild, A.; Grätzel, M.; Mathews, N. Enhancement in the Performance of Ultrathin Hematite Photoanode for Water Splitting by an Oxide Underlayer. *Adv. Mater.* **2012**, *24* (20), 2699−2702.
(24) Terashima, K.; de Castro, P. B.; Saito, A. T.; Yamamoto, T. D.; Matsumoto, R.; Takeya, H.; Takano, Y. Experimental Exploration of ErB2 and SHAP Analysis on a Machine-Learned Model of Magnetocaloric Materials for Materials Design. *Sci. Technol. Adv. Mater.: Methods* **2023**, *3* (1), No. 2217474.
(25) Lundberg, S.; Lee, S.-I. A Unified Approach to Interpreting Model Predictions. 2017, arXiv:1705.07874. arXiv.org e-Printarchive. https://arxiv.org/abs/1705.07874.
(26) Zhu, J.; Ng, K. Y. S.; Deng, D. Micro Single Crystals of Hematite with Nearly 100% Exposed {104} Facets: Preferred Etching and Lithium Storage. *Cryst. Growth Des.* **2014**, *14* (6), 2811−2817.
(27) Chan, J. Y. T.; Ang, S. Y.; Ye, E. Y.; Sullivan, M.; Zhang, J.; Lin, M. Heterogeneous Photo-Fenton Reaction on Hematite (α-Fe2O3) {104}, {113} and {001} Surface Facets. *Phys. Chem. Chem. Phys.* **2015**, *17* (38), 25333−25341.
(28) Shinde, P. S.; Choi, S. H.; Kim, Y.; Ryu, J.; Jang, J. S. Onset Potential Behavior in α-Fe2O3 Photoanodes: The Influence of Surface and Diffusion Sn Doping on the Surface States. *Phys. Chem. Chem. Phys.* **2016**, *18* (4), 2495−2509.
(29) Patra, A. K.; Kundu, S. K.; Bhaumik, A.; Kim, D. Morphology Evolution of Single-Crystalline Hematite Nanocrystals: Magnetically Recoverable Nanocatalysts for Enhanced Facet-Driven Photoredox Activity. *Nanoscale* **2016**, *8* (1), 365−377.
(30) Bisquert, J. *Nanostructured Energy Devices.*.
(31) Rioult, M.; Magnan, H.; Stanescu, D.; Barbier, A. Single Crystalline Hematite Films for Solar Water Splitting: Ti-Doping and Thickness Effects. *J. Phys. Chem. C* **2014**, *118* (6), 3007−3014.
(32) Pu, A.; Deng, J.; Li, M.; Gao, J.; Zhang, H.; Hao, Y.; Zhong, J.; Sun, X. Coupling Ti-Doping and Oxygen Vacancies in Hematite Nanostructures for Solar Water Oxidation with High Efficiency. *J. Mater. Chem. A* **2014**, *2* (8), 2491−2497.
(33) Inaba, M.; Katayama, K.; Sohn, W. Y. Cooperative Effects of Surface and Interface Treatments in a Hematite (α-Fe2O3) Photo-Anode on Its Photo-Electrochemical Performance. *Sustainable Energy Fuels* **2020**, *4* (5), 2174−2183.
(34) Idei, T.; Pan, Z.; Katayama, K. Combined Effect of Underlayer and Deposition Solution to Optimize the Alignment of Hematite Photoanodes. *Langmuir* **2024**, *40*, 11526−11533, DOI: 10.1021/acs.langmuir.4c00621.

https://doi.org/10.1021/acsomega.4c08633
ACS Omega 2024, 9, 44837−44845